Afterpulsing Effects in Free-Running InGaAsP Single-Photon Avalanche Diodes

Xudong Jiang, Mark A. Itzler, *Senior Member, IEEE*, Rafael Ben-Michael, Krystyna Slomkowski, Michael A. Krainak, Stewart Wu, and Xiaoli Sun

***Abstract*—We demonstrate large-area (80 μm diameter) InP-based single-photon avalanche diodes for Geiger-mode operation at 1.06 μm with dark count rates of $\sim$1000 Hz at high detection efficiencies of 30% at 237 K, as well as simulations of dark count rate and detection efficiency that provide good agreement with measured data. Experimental results obtained using free-running operation illustrate the strong impact of afterpulsing effects for short ($\sim$200 ns) hold-off times. We present an analysis of these free-running results that quantifies the contribution of afterpulsing to the total count rate.**

***Index Terms*—Avalanche photodiodes, photodiodes, single-photon avalanche diodes, single photon detection.**

I. Introduction

SINGLE-PHOTON detection at 1.06 μm is of considerable importance for ladar and lidar systems designed for remote sensing and ranging [1], as well as for free-space optical communications in photon-starved environments [2]. Silicon single-photon avalanche diodes (SPADs) offer excellent performance for single-photon detection in the visible spectral range, but they suffer from a dramatic reduction in single-photon detection efficiency for wavelengths beyond 1 μm, and detection efficiencies do not exceed a few percent at 1.06 μm. The rapid development of quantum key distribution and other applications employing single-photon detection at telecommunication wavelengths of $\sim$ 1.5 μm has instigated significant progress in InGaAs–InP SPADs [3]–[11]. However, the relatively narrow bandgap of the InP-lattice-matched $In_{0.53}Ga_{0.47}As$ absorber, used to achieve a long-wavelength cutoff of $\sim$ 1.65 μm for the InGaAs–InP device, leads to relatively high dark count rates. This performance tradeoff is unnecessary if detection of these longer wavelengths is not desired.

To bridge the "single-photon detection gap" for wavelengths just beyond 1 μm, we have developed large-area (80–200 μm diameter) InP-based InGaAsP quaternary absorber SPADs optimized for operation at 1.06 μm that are based on a highly reliable planar geometry avalanche photodiode structure [8]. For single-photon detection at 1.06 μm, SPADs based on the InGaAsP quaternary material system are likely to provide the most appropriate solution in numerous situations in which sufficiently high performance must be accompanied by high reliability, compact form factor, ease of use, and acceptable cost. However, relative to the body of work dedicated to 1.5-μm InGaAs–InP SPADs, there has been minimal focus to date on InGaAsP–InP SPADs for 1.06 μm. (A notable exception is the substantial work done by researchers at MIT Lincoln Laboratory on related small-area mesa-geometry devices [12]–[15].) In this paper, we demonstrate large 80-μm-diameter devices that provide detection efficiency at 1.06 μm (e.g., 30%) that exceeds that of Si SPADs by more than an order of magnitude while maintaining low dark count rates (of the order of 1000 Hz) at temperatures that are readily accessible using compact thermoelectric coolers.

In this study, we have also stressed the importance of identifying performance limitations and constraints on the applicability of these devices. With the goal of employing these devices in high-count-rate free-running operation, we have characterized their behavior at submicrosecond hold-off times and have found that afterpulsing dominates the total count rate for very short hold-off times of $\sim$200 ns at a typical operating temperature of 230 K, even for very low overbias values in the range of 0.1 to 0.4 V. We present an analysis in which we quantify afterpulsing effects under these measurement conditions and extract intrinsic signal count and dark count rates. Through this analysis, we have clarified an earlier report of these data [16] in which the role of afterpulsing had not yet been quantified.

The remainder of this paper is organized as follows. In Section II, we briefly describe our InGaAsP–InP 1.06-μm SPAD device structure. In Section III, we present simulations for the dark count rate versus detection efficiency behavior of these devices and summarize the principle dark carrier generation mechanisms contributing to the dark count rate. Experimental results for gated measurements are presented in Section IV and establish the baseline for device performance. In Section V, we present experimental data for free-running measurements along with a relevant analysis to quantify afterpulsing effects. Results are discussed and conclusions are summarized in Section VI.

II. Device Structure

SPADs are avalanche photodiodes designed to operate at biases beyond their breakdown voltage, in the so-called "Geiger mode," for which the photoexcitation of a single carrier can produce a self-sustaining avalanche. This runaway avalanche

Manuscript received June 1, 2007; revised July 30, 2007. This work was supported in part by the National Aeronautics and Space Administration under Grant NNG06LA04C.

X. Jiang, M. A. Itzler, R. Ben-Michael, and K. Slomkowski are with Princeton Lightwave Inc., Cranbury, NJ 08512 USA (e-mail: xjiang@princetonlightwave.com; mitzler@princetonlightwave.com; rben-michael@princetonlightwave.com; kslomkowski@princetonlightwave.com).

M. A. Krainak, S. Wu, and X. Sun are with the NASA Goddard Space Flight Center, Greenbelt, MD 20771 USA (e-mail: Michael.A.Krainak@nasa.gov; swu@pop500.gsfc.nasa.gov; xsun@pop900.gsfc.nasa.gov).

Color versions of one or more of the figures in this paper are available online at http://ieeexplore.ieee.org.

Digital Object Identifier 10.1109/JQE.2007.906996

0018-9197/$25.00 © 2007 IEEE

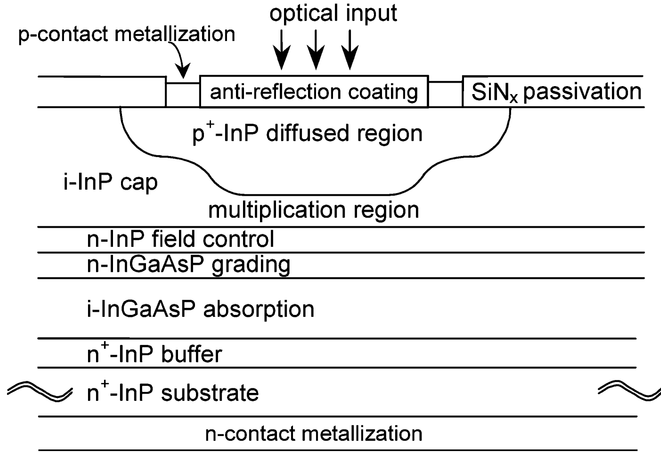

Fig. 1. Schematic cross section of front-illuminated InGaAsP–InP SPAD structure for single-photon detection at 1.06 μm.

gives rise to a macroscopic current pulse which can be sensed using an appropriate threshold detection circuit. Critical SPAD performance parameters include the photon detection efficiency (PDE), the dark count rate (DCR), and the afterpulsing probability (AP). Material quality, device design, and operating conditions can all affect these parameters. A primary goal of SPAD device design is to minimize DCR while maximizing PDE by optimization of the device structure and the resulting internal avalanche diode electric field profile.

Our 1.06-μm SPAD employs a device design platform similar to the planar geometry avalanche diode structure we have used in fabricating 1.55-μm InGaAs–InP SPADs, as described in detail in [8]. As illustrated in Fig. 1, the structure consists of a separate absorption, grading, charge, and multiplication (SAGCM) layer scheme. Avalanche gain occurs via impact ionization in an undoped InP multiplication layer. The role of the InP charge, or field control, layer is to maintain a high electric field in the multiplication region to generate avalanche gain while maintaining a low field in the absorption layer to reduce carrier tunneling. Grading layers are used to smooth out the abrupt heterointerface band offset that would result if the absorber and an InP field control layer were immediately adjacent.

A primary difference between the 1.55- and 1.06-μm SPADs lies in the material used for the absorber layer: the former consists of InGaAs lattice-matched to InP, while the latter employs quaternary InGaAsP lattice-matched to InP with a 295 K cutoff wavelength of $\sim$1200 nm. With a larger bandgap absorber in the 1.06-μm SPAD, the dark counts related to dark carriers generated in the absorption layer via thermal generation-recombination process can be reduced. However, to take full advantage of potential performance improvements, the entire vertical structure of the device (and the associated internal electric field profile) must be reengineered relative to the 1.55-μm SPAD design [8]. Device simulations in the following section illustrate how design choices for critical elements in the SPAD structure, such as the multiplication region width, affect device performance.

III. Device Performance Simulation

Numerous mechanisms generate electrical carriers in a SPAD structure. Electron—hole pair generation by photon absorption in the InGaAsP absorption layer is the desired carrier generation mechanism, but in addition to photoexcited carriers, dark carrier generation by various thermal and tunneling processes in multiple layers of the structure can be significant. In Geiger mode operation, all electrical carriers have a finite probability P_a of creating a detectable current pulse by initiating an avalanche event in the multiplication region.

The thermal generation rate is determined principally by Shockley–Read–Hall (SRH) processes. In the depletion region, they are determined by the intrinsic carrier concentration n_i and SRH lifetime τ_{SRH}. Tunneling processes include direct band-to-band tunneling (BBT) and trap-assisted tunneling (TAT). BBT is determined by the bandgap energy, electric field intensity, and the reduced mass of conduction band and light-hole-band effective masses. TAT depends primarily on the electric field, the position of traps inside the bandgap, and the trap density. Formulas for these different dark carrier generation mechanisms in the context of InGaAsP SPADs have been reviewed by Donnelly *et al.* [13], and we have adopted the formalism of these authors for the following simulations.

For the calculation of breakdown voltage, we adopted the physical model of Zappa *et al.* [17] for temperature-dependent ionization coefficients. For appropriately designed InP-based SPADs, multiplication layer widths are sufficiently thick ($\geq 1\ \mu$m) that dead space effects, which are important for APDs with thin multiplication layers, can be ignored. For the calculation of quantum efficiency, the model of Adachi [18] was used to calculate wavelength-dependent absorption coefficients, and the effects of electroabsorption [19] and free-carrier absorption have also been included. For the calculation of avalanche probability P_a, McIntyre's model [20] was used.

The effective mass of electrons and holes and the change of bandgap energy with temperature were taken from [21]. Following Donnelly *et al.* [13], we define a parameter $\alpha = (E_{\mathrm{trap}} - E_v)/E_g$ to identify the position of traps inside the energy bandgap, where E_g is the bandgap energy, E_{trap} is the energy level of the trap, and E_v is the top of the valence band. α is taken to be $\sim$0.78 for $\mathrm{In_{0.53}Ga_{0.47}As}$ [22] and $\sim$0.75 for InP [23]. A linear interpolation based on the energy bandgap of each layer is used to obtain the trap energy level in InGaAsP quaternary layers. The SRH lifetime τ_{SRH} and trap concentrations N_{trap} are obtained from the fitting of simulated results to experimental results. For τ_{SRH}, we obtained 70 μs; this relatively large value indicates good material quality. For trap densities, we obtained $N_{\mathrm{trap}}(\mathrm{In_{0.53}Ga_{0.47}As}) \sim 1\times10^{15}$ cm^{-3} and $N_{\mathrm{trap}}(\mathrm{InP}) \sim 2\times10^{14}$ cm^{-3}. The trap concentrations in layers other than InP and $\mathrm{In_{0.53}Ga_{0.47}As}$ are estimated using linear interpolations between the values just cited based on the bandgap energy of the quaternary layer.

Our primary goal is to minimize DCR while maximizing PDE. An effective method for displaying results and comparing different designs is to plot curves for DCR as a function of PDE. Many device parameters will affect the DCR versus PDE performance metric, but, among these parameters, the multiplication layer thickness d_M is particularly important.

Fig. 2 shows the calculated DCR per unit area versus detection efficiency with different multiplication layer thickness for 1.06-μm wavelength SPADs at $T = 230$ K [Fig. 2(a)] and

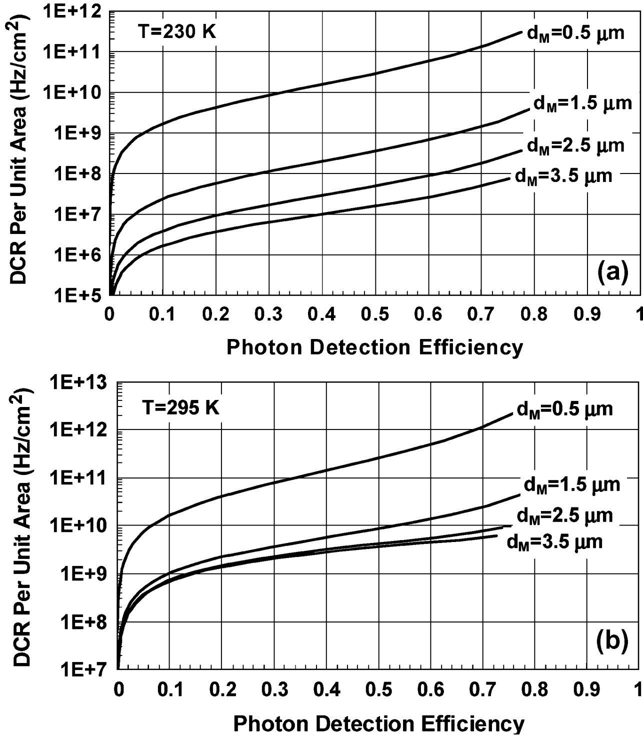

Fig. 2. Calculated DCR per unit area versus PDE for different multiplication layer thickness d_M for 1.06-μm InGaAsP–InP SPADs at (a) 230 K and (b) 295 K.

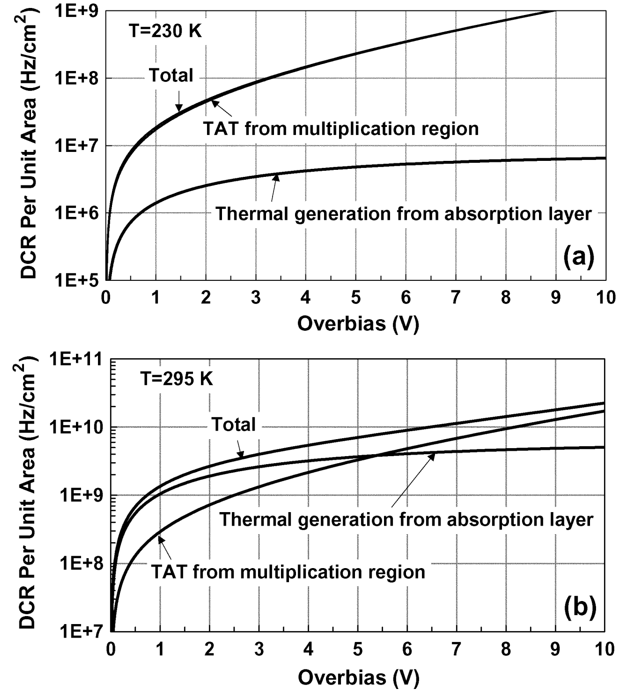

Fig. 3. Calculated dependence of DCR per unit area versus overbias for 1.06-μm SPAD at (a) 230 K and (b) 295 K. The total DCR per unit area and contributions to DCR from multiplication layer TAT and absorption-layer thermal generation process are shown. In (a), DCR from the multiplication-layer TAT dominates completely and is indistinguishable from the total DCR.

$T = 295$ K [Fig. 2(b)]. For a given detection efficiency, the DCR decreases as d_M increases, and the decrease of DCR with increasing d_M becomes less significant as d_M increases. At 230 K, DCR continues to decrease as d_M is increased from 2.5 μm to 3.5 μm, while at 295 K, DCR versus PDE shows little difference between $d_M = 2.5$ μm and $d_M = 3.5$ μm.

For low temperatures (e.g., 230 K), the dominant dark carrier generation mechanism in the 1.06-μm SPAD is TAT in the multiplication region. TAT is very sensitive to electric field intensity, and, for larger multiplication layer thickness d_M, the electric field required to produce a desired avalanche probability P_a decreases. Therefore, for a given PDE (which is dictated by the product of P_a and the absorption region quantum efficiency η), larger values of d_M result in a decrease in TAT. Because the dependence of P_a on electric field becomes weaker as d_M increases, progressively larger values of d_M provide finite but progressively smaller improvements in the trap-assisted tunneling dark carrier generation rate, as seen in Fig. 2(a).

For sufficiently high temperatures (e.g., 295 K), dark carrier generation in the absorption region becomes important. Since thermal generation is insensitive to electric field, the increase of d_M has less impact on DCR than it does at low temperature. Consequently, for the structures simulated, the DCR dependence on PDE is essentially unchanged for $d_M > 2.5$ μm, as seen in Fig. 2(b). Based on these simulations, we have chosen a multiplication layer width of 1.7 μm for our experimental device structures.

To more clearly illustrate the roles of the dominant dark count generation mechanisms in the 1.06-μm SPAD, we present in Fig. 3 the calculated dependence on overbias of the total DCR as well as the two most important contributions to DCR, i.e., TAT in the multiplication layer and thermal generation in the absorption layer. Calculations assumed a multiplication layer thickness of 1.75 μm and are presented for temperatures of 230 K and 295 K. As can be seen from this figure, at 230 K, the TAT from the multiplication layer completely dominates the total DCR. At 295 K, both TAT in the multiplication layer and thermal generation in the absorption layer play important roles. For overbias values less than ~5 V, thermal generation in the absorption layer is the larger contributor to the total DCR. At overbias values greater than ~5 V, TAT in the multiplication layer is more significant. The interplay between TAT and thermal generation at different temperatures and overbiases is central to understanding the behavior of the total DCR in various operating conditions, as already seen in our discussion of the simulations of DCR versus PDE presented in Fig. 2. In these simulations, we have also considered the DCR contributions from other layers of the structure (e.g., the field control and grading layers), but these were found to be negligible compared with the contributions from the absorption and multiplication layers. Band-to-band tunneling was also evaluated in all layers and found to be negligible.

A similar analysis can be done for 1550-nm SPADs as well, and the result will be qualitatively similar to what is described in Figs. 2 and 3 for 1064-nm SPAD. The only difference is that the thermal generation rate from the absorption region will be larger, and the low-temperature thermal generation rate from the absorption region will still have a significant contribution, whereas in 1064-nm SPADs it is totally dominated by TAT from the multiplication region.

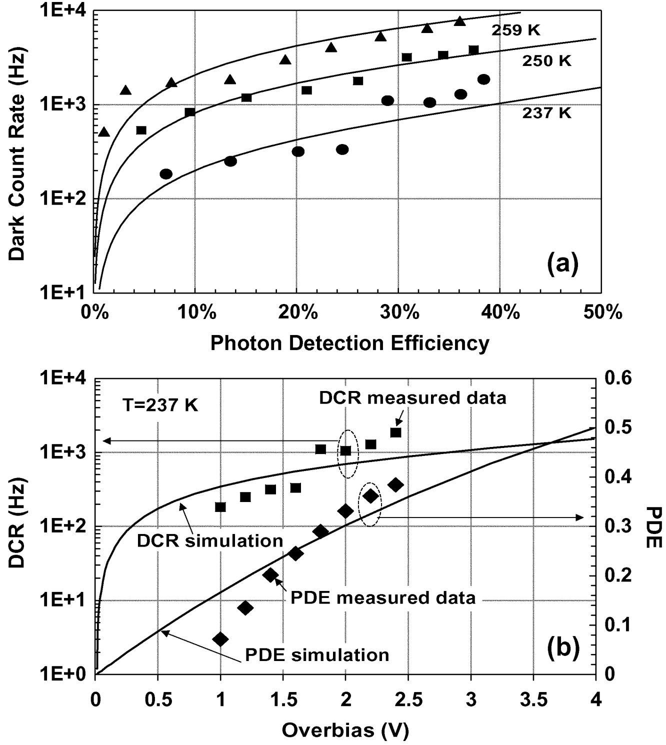

Fig. 4. (a) DCR versus PDE of an 80-μm-diameter InGaAsP SPAD measured at 237 K (circles), 250 K (squares), and 259 K (triangles) in 1-ns gated-mode operation at 500-kHz repetition rate using a 1.06-μm pulsed diode laser source. Simulation results at the three temperatures (solid lines) are also shown. (b) Dependence of DCR and PDE on overbias at 237 K for measured (symbols) and simulated (solid line) results.

IV. Experimental Results: Gated Measurements

We directly measured DCR versus PDE using a gated-mode measurement technique with short 1-ns gates at a repetition rate of 500 kHz. With this setup, we employ a scheme in which "lit" and "dark" gates are interleaved so that DCR, PDE, and afterpulsing can be measured [9], [24]. When this setup is operated with the source laser turned off, all of the observed counts are dark counts. To obtain PDE and afterpulsing data, a pulsed diode laser source is synchronized so that single photons are temporally coincident only with the "lit" gate pulses; for the sake of clarity, we define all odd gates as "lit" gates and all even gates as "dark" gates. A 1.06-μm laser source is attenuated to generate a mean photon number of $\mu = 0.1$ per "lit" gate pulse, with a pulse full-width at half-maximum (FWHM) of 500 ps.

The DCR is obtained by measuring the dark count probability per gate in the absence of input photons. The PDE is determined by monitoring the total number of counts occurring in the odd "lit" gates when the single-photon source is activated. During these lit measurements, an increase in the count rate found for the even "dark" gates (which are interleaved between the "lit" gates) above the intrinsic DCR indicates the presence of afterpulsing and can be used to quantify the afterpulse probability per gate.

Using this short-gate measurement technique, we obtained the experimental data presented in Fig. 4(a) (circles, squares, and triangles for $T = 237$, 250, and 259 K, respectively) for DCR versus PDE for an 80-μm-diameter 1.06-μm SPAD. For a PDE of 30%, DCR values of $\sim$1 kHz can be obtained at 237 K with 2-V overbias. These data are in reasonable agreement with simulation results (solid lines) obtained from the modeling approach outlined in Section III. For the 500-kHz repetition rate used (i.e., 2 μs hold-off time between 1-ns gates), the afterpulse probability per 1-ns gate was found to be less than 10^{-4} for PDE values as large as $\sim$35%. Fig. 4(b) shows the dependence of DCR and PDE on overbias at 237 K.

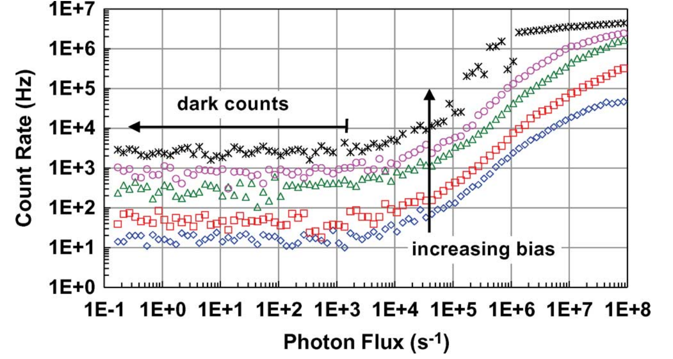

Fig. 5. Free-running count rate versus incident photon flux at 1.06 μm for an 80-μm-diameter InGaAsP SPAD at 230 K for five different bias voltages between 0.1 and 0.4 V using an active quench circuit with a 200-ns hold-off time.

V. Experimental Results: Nongated Measurements

A. *Free-Running Count Rate versus Photon Flux*

For many applications of single photon counting at 1.06 μm, free-running operation is highly desirable. For instance, in lidar and remote sensing measurements [1], the timing of reflected pulses from soft targets cannot be synchronized to the pulse launch, and detector gating is therefore inappropriate. Moreover, the goal of having the detector active as much of the time as possible dictates the need for very short "dead times" (or hold-off times) between a detection event and the subsequent re-arming of the device.

To evaluate the InGaAsP SPADs relative to these requirements, we obtained free-running measurement data using a Poisson source of 1.06-μm photons, the InGaAsP SPAD detector, and appropriate backend electronics. A commercially available active quenching circuit (AQC) described in [25] was used, and photon flux was calibrated using a reference Si-based SPAD detector. The essence of the technique was to measure total count rate as a function of incident photon flux, which was swept over a wide range from 10^{-1} to 10^{8} photons/s. To our knowledge, this measurement technique has not been reported previously in the photon counting literature.

Fig. 5 shows the dependence of the free-running count rate on the incident photon flux for the 80-μm-diameter 1.06-μm SPAD under five different overbias values between 0.1 and 0.4 V at 230 K with the AQC set to a 200 ns hold-off time. The constant count rate for low photon fluxes ($< 10^{3}$ s^{-1}) is due to dark counts. For flux values larger than $\sim 10^{4}$ s^{-1}, the count rate increases roughly linearly with photon flux and is dominated by signal counts. We can define the raw signal count efficiency $\mathrm{RSCE} \equiv (R_t - R_d)/\phi$, where R_t, R_d, and ϕ are the total count rate, raw DCR, and photon flux, respectively. Using values for R_t at

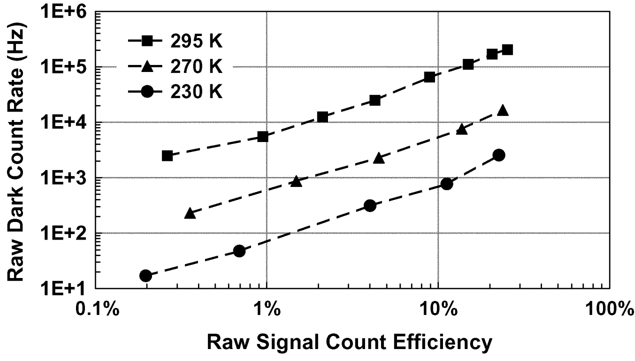

Fig. 6. Raw DCR versus raw signal count efficiency for a 1.06-μm SPAD. Experimental data at 295 K (squares), 270 K (triangles), and 230 K (circles) were extracted from count rate versus photon flux measurements (as shown in Fig. 5 for the 230 K data).

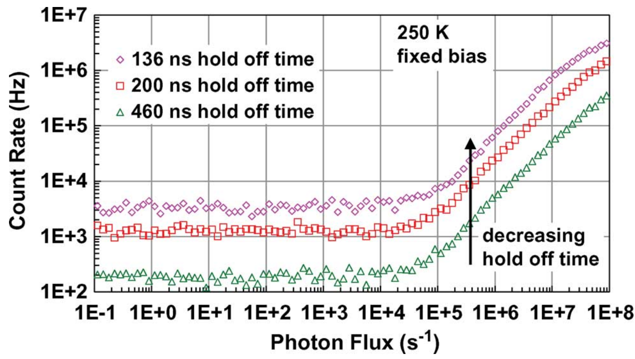

Fig. 7. Count rate versus photon flux measured at 250 K at fixed overbias with three different hold-off times set for the active quench circuit.

$\phi \sim 10^6$ s^{-1}, the relationship between R_d and RSCE is plotted in Fig. 6, where we have also included data obtained at 270 K and 295 K for the same device. Because the total count rate R_t contains counts due to afterpulsing, we cannot simply equate R_d with the intrinsic DCR and RSCE with the detection efficiency. In fact, we will show that, for the operating conditions cited, the contribution of afterpulses is very significant, and R_d (RSCE) exceeds DCR (DE) by a considerable factor.

B. Dependence of Count Rate on Hold-Off Time

A SPAD avalanche event generally consists of the flow of a large number of carriers (e.g., 10^7 to 10^8) through the multiplication layer of the device. Material defects in this layer can temporarily trap carriers, and the de-trapping of these carriers at a later time can initiate subsequent avalanche events (referred to as afterpulses) if the de-trapping occurs after the SPAD has been rearmed. Afterpulsing can be mitigated by using long hold-off times which allow sufficient time for trapped carriers to be de-trapped and swept out of the multiplication region before the SPAD is rearmed; however, long hold-off times preclude high repetition rates. Conversely, the shorter the hold-off time is, the worse the afterpulsing effects are.

To explore the role of afterpulsing in our count rate versus photon flux measurements, we repeated these measurements for a single fixed overbias value with different hold-off times set for the active quench circuit. Fig. 7 shows data obtained at 250 K for three different hold-off times of 136, 200, and 460 ns. Even for this somewhat limited range of hold-off times (imposed by constraints of our apparatus), the impact of hold-off time on count rate at a given photon flux is dramatic. In particular, when the hold-off time is increased from 200 to 460 ns, the count rate decreases by approximately five to six times for all photon flux values. This clearly indicates that a large fraction of counts in the 200-ns hold-off time measurement are due to afterpulses.

To quantify the contribution of afterpulsing to the total count rate, we have performed the following analysis. We begin by assuming that the measured total count rate R_t can be expressed as [14]

$$R_t = R_{\rm di} + R_{\rm pi} + R_{\rm ap}(t) \tag{1}$$

where $R_{\rm di}$, $R_{\rm pi}$, and $R_{\rm ap}(t)$ are the intrinsic (afterpulse-free) DCR, the intrinsic (afterpulse-free) photon count rate, and the time-dependent afterpulse count rate, respectively. Note that $R_{\rm di}$ and some portion of $R_{\rm ap}(t)$ combine to give the raw DCR R_d specified in the previous section; likewise, $R_{\rm pi}$ and some portion of $R_{\rm ap}(t)$ combine to give the raw signal count rate R_s. Ultimately, $R_{\rm pi}$ can be converted to the PDE.

Assuming that afterpulsing is dominated by a single type of trap, $R_{\rm ap}(t)$ can be written as [14]

$$R_{\rm ap}(t) = C_0 \exp\left[-(t + T_{\rm ho})/\tau_d\right] \tag{2}$$

where C_0 is a prefactor depending on the total current flow, and $T_{\rm ho}$ and τ_d are the hold-off time and characteristic de-trapping time, respectively. Performing an ensemble average, we can obtain the observed afterpulsing

$$R_{\rm ap} = \langle R_{\rm ap}(t)\rangle = C_0 \exp(-T_{\rm ho}/\tau_d)\,\langle \exp(-t/\tau_d)\rangle\,. \tag{3}$$

Denoting $C \equiv C_0\langle \exp(-t/\tau_d)\rangle$, we find $R_{\rm ap} = {\rm C}\exp(-{\rm T}_{\rm ho}/\tau_d)$, and we can use this formula to fit experimental data to extract parameters $R_{\rm di}$, C, τ_d, and $R_{\rm pi}$ by the following procedure.

Step 1) Use the low photon flux ($\phi < 10^3$ s^{-1}) count rate data at three different hold-off times to obtain $R_{\rm di}$, C, and τ_d for the dark count case.

Step 2) Use the high flux ($\phi > 10^4$ s^{-1}) data at three different hold-off times to obtain C, τ_d, and $R_o = R_{\rm pi} + R_{\rm di}$ for any particular ϕ.

Step 3) Obtain the intrinsic photon count rate $R_{\rm pi} = R_o - R_{\rm di}$ by subtracting from R_o the contribution of DCR $R_{\rm di}$ which was obtained from step 1). The detection efficiency is then given by ${\rm DE} = R_{\rm pi}/\phi$, where ϕ is the photon flux at which $R_{\rm pi}$ was taken.

In Fig. 8, we provide the extracted de-trapping time τ_d (squares) and pre-factor C (diamonds) at four different photon fluxes. To within experimental error, the de-trapping time is independent of photon flux, as expected, and is found to be ~65 ns, which is indicated by the dashed line. The results for pre-factor C show that it exhibits an approximately linear increase—i.e., power law with a slope of nearly 1—with photon flux (solid line). This finding is consistent with C_0 being proportional to the total current flow through the SPAD

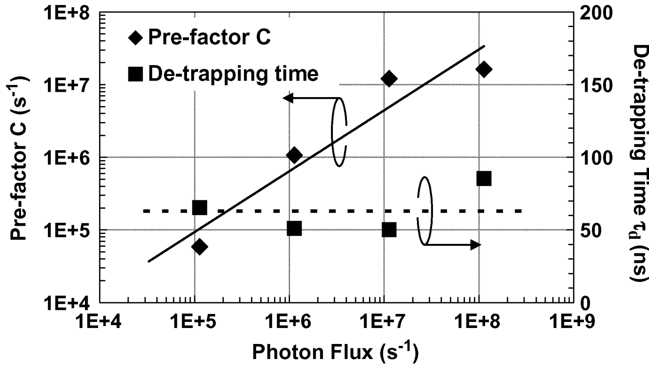

Fig. 8. Extracted pre-factor C (diamonds, left axis) and de-trapping time (squares, right axis) at four different photon fluxes based on analysis of data in Fig. 7; see the text for details.

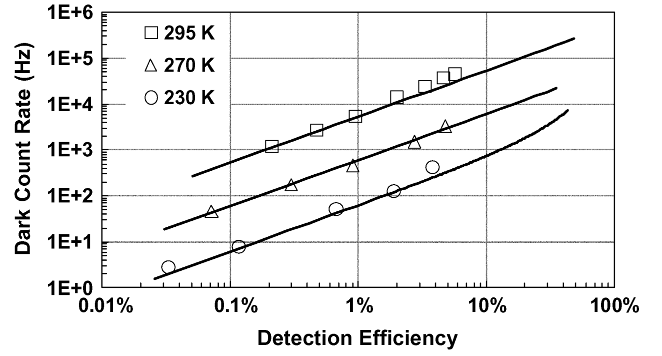

Fig. 10. Intrinsic DCR versus DE at 295 K (squares), 270 K (triangles), and 230 K (circles), obtained by a renormalization procedure described in the text for eliminating the effects of afterpulsing. Solid lines are simulated results for the three temperatures.

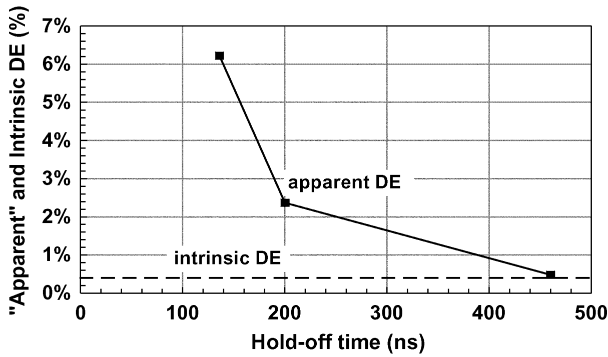

Fig. 9. "Apparent" detection efficiencies for three different hold-off times using 250 K data from Fig. 7. Also shown is the extracted intrinsic detection efficiency (dashed line). At each hold-off time, the apparent DE is the average value for measurements made at four different photon flux values.

structure, since this total current flow will be proportional to the photon flux. (Although the data points at $\phi = 10^7$ and $\phi = 10^8$ demonstrate a roll-off in pre-factor C that could be consistent with trap saturation, we do not believe that this degree of trap filling is likely; instead, uncertainty in the measurement and the analysis is the more probable explanation for the observed nonlinear dependence.)

It is worth noting that our use of a single trap model ignores the possibility of additional contributions to $R_{\rm ap}$ from defects with a longer de-trapping time τ_d. Given the narrow range and very short values of the hold-off times used in our measurements, afterpulsing from defects with substantially longer τ_d will contribute a fairly constant "background" that would be interpreted as part of our intrinsic DCR. The analysis can be extended to multiple trap models if data can be obtained for a sufficiently wide range of hold-off times.

With calculated values for pre-factor C and de-trapping time τ_d at specific hold-off times $T_{\rm ho}$, we can use (3) to obtain the average afterpulsing $R_{\rm ap}$ for each $T_{\rm ho}$. By using $R_{\rm ap}$ in place of $R_{\rm ap}(t)$ in (1), we can calculate, for each of the four values of ϕ used above, an "apparent" detection efficiency for each $T_{\rm ho}$. The apparent detection efficiency should have no dependence on ϕ; therefore, we simply average the extracted four values to arrive at a more accurate estimate of apparent DE for each $T_{\rm ho}$, as illustrated in Fig. 9. In addition to data for the three experimental hold-off times, we also show the extracted intrinsic DE, indicated by the dashed line at $\sim$0.4%. The results in Fig. 9 suggest that a correction factor is needed at each hold-off time to convert the "apparent" DE to the intrinsic DE. At a hold-off time of 200 ns, this correction factor is $\sim$5–6.

As a final step in our analysis to correct for afterpulsing effects, we can use the correction factors just described with reference to Fig. 9 to convert the raw DCR versus raw signal count effficiency data (presented in Fig. 6) to intrinsic DCR versus DE curves. Inasmuch as the afterpulsing effects are temperature-dependent, these correction factors (which describe the severity of afterpulsing) should also be temperature-dependent. For the data at 230 K, 270 K, and 295 K, we obtain the intrinsic DCR versus DE curves (shown in Fig. 10) using correction factors of 6.0, 5.0, and 4.5, respectively. The open symbols are the renormalized experimental data at the three different temperatures. Also shown in this figure are DCR versus DE simulations obtained for the three corresponding temperatures using the methodology outlined in Section III. The model provides a good fit for the intrinsic DCR versus DE.

The parameters for fitting the intrinsic DCR versus DE in Fig. 10 are the same as those used to fit the short-gate measurement results in Section IV (see Fig. 4), with the exception that the trap position parameter α at the lowest temperature (e.g., 230 K) has been shifted by about 5%. Considering that trap position may change slightly with temperature, this adjustment for α at 230 K is reasonable. The modeling done in this section and the previous section show that the short-gate measurement data and the normalized free-running data can be described by the same set of device model parameters and are therefore consistent with each other.

C. Laser Pulse Histogram and Ranging

The significant afterpulsing in both dark and signal count rates found when the 1.06-μm SPAD is operated using short (e.g., 200 ns) hold-off times needs to be further evaluated with respect to intended applications such as ranging. To this end, we have used a laser pulse histogram method in which a fast laser generates a narrow temporal width (FWHM $\sim$60 ps), low-jitter (rms jitter $\sim$10–20 ps) optical pulse that is incident on the 1.06-μm SPAD. The response of the SPAD is registered with a multichannel scalar, which records the presence or absence

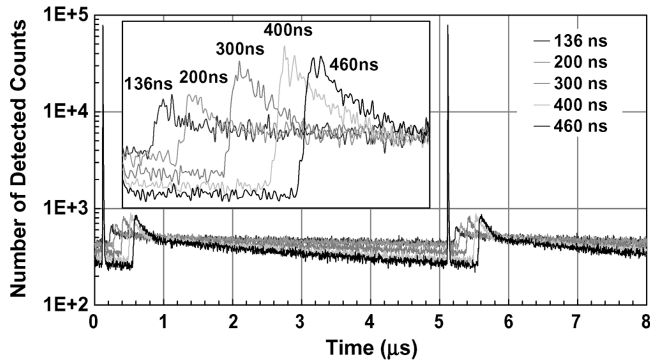

Fig. 11. Laser pulse histogram data for a free-running 80-μm-diameter InGaAsP SPAD, operated at five different hold-off times, constructed using a multichannel scalar with 4-ns time bins. The inset shows in more detail the initial portion of the histogram immediately after the main peak.

of counts in short time bins. The results of measurements employing a bin width of 4 ns and five different hold-off times are shown in Fig. 11.

The effect of afterpulsing and hold-off time can be clearly seen in Fig. 11. A main peak of ~80 000 counts is induced by the laser pulse itself, and side peaks consisting of long decaying tails are caused by afterpulsing. The spacing between the main peak and the side peaks directly reflects the hold-off time used. The result presented here also shows that, even in the presence of considerable afterpulsing, the 1.06-μm SPAD can still clearly distinguish between two peaks and, therefore, can be used for laser ranging to hard targets. The key issue here is the range resolution, which is limited by the hold-off time. Optimizing the operating conditions can help to increase the resolution.

VI. Discussion and Conclusion

From short-gate measurements, we have found that our large-area (80μm diameter) 1.06-μm SPADs provide an intrinsic DCR of ~1 kHz at a high detection efficiency of 30% for a temperature (237 K) easily attained using thermoelectric coolers (TECs). This is also confirmed by our free-running measurements, although the intrinsic DE achieved in these measurements was limited to <10% due to the very sizable contribution of afterpulsing effects found for the short (~200 ns) hold-off times used. With slightly more aggressive cooling (still accessible using TECs), the DCR performance of this device is competitive with that of commercial Si SPADs for a PDE that exceeds that of Si SPADs by more than an order of magnitude.

Our experimental results for intrinsic DCR versus DE agree well with the output of our device performance simulations. In addition to confirmation of experimental data, these simulations also provide insights into the different mechanisms contributing to DCRs. For low-temperature operation at 230 K, the DCR is dominated by TAT in the multiplication region. For high-temperature operation at 295 K, both multiplication-region TAT and absorption region thermal generation are significant, with the latter component proving to be more important at low overbias and the former component taking over at high overbias.

In this study, we have quantified the very significant contribution of afterpulses to both dark count and signal count rates for very short hold-off times using an analysis to extract the afterpulse count rate under various operating conditions. For data obtained at 250 K and short hold-off times of 200 ns, we have shown that nearly five out of every six counts in the raw total count rate are afterpulses. Through this analysis, we also show that a very substantial reduction in afterpulsing is realized by increasing the hold-off time from 200 ns to ~500 ns. The assumption of a single trap model in our analysis leaves open the possibility that additional afterpulsing due to longer lifetime traps (i.e., traps with larger τ_d) may still be contributing to the nominally intrinsic DCR derived from the analysis. However, we believe that any remaining afterpulse contributions are small because: 1) the renormalized data are fit well by our (afterpulse-free) simulations and 2) the renormalized data provide reasonable agreement with the DCR versus DE data obtained from the short-gate measurements described in Section IV, for which the afterpulsing was confirmed to be small.

Nevertheless, it is highly desirable to operate SPADs with hold-off times shorter than 500 ns. A hold-off time of this duration restricts usable repetition rates to ~2 MHz and limits range resolution in ranging applications. To some extent, limitations imposed by afterpulsing can be mitigated by altering device operating conditions (e.g., operation at higher temperature or lower bias), but this approach often results in performance trade-offs (e.g., higher intrinsic DCR or lower DE). Therefore, careful application-dependent optimization should be carried out. Another approach to reducing hold-off times with existing SPADs is to use multiple devices—for instance, through the use of multi-pixel arrays [14]—so that while one device is disarmed after detecting a photon, all the other devices remain armed and capable of detecting additional photons incident at a rate much greater than the rearming cycle of a single device. The drawbacks of this approach are the much greater complexity of fabricating arrayed devices, the design of an appropriate readout integrated circuit for this concept, and the fabrication of the resulting focal plane array.

Improvement in materials properties that give rise to afterpulsing—such as reduction in the density of trap defects in the multiplication region—is a more direct approach to boosting device performance, but little is known at present about the nature of these traps, and more fundamental work is needed to address materials issues. Perhaps the greatest near-term promise lies in more suitable device or circuit designs that enable SPAD operation with greatly reduced current flow associated with each avalanche event. Since the number of trapped charges is directly proportional to the charge flow through the device, afterpulsing should be greatly improved if charge flow can be substantially reduced.

Acknowledgment

The authors would like to thank B. Nyman and M. Entwistle for assistance with the short-gate measurements and related discussions.

References

[1] R. M. Measures, *Laser Remote Sensing: Fundamentals and Applications*. New York: Wiley, 1984.

[2] "Special issue on 'Free-space communication techniques for optical networks'," *IEEE LEOS Newslett.*, vol. 19, no. 5, pp. 6–39, Oct. 2005.

[3] "Special issue on 'Single-photon: Detectors, applications, and measurement methods'," *J. Mod. Opt.*, vol. 51, no. 9–10, Jun. 2004.

[4] A. Lacaita, F. Zappa, S. Cova, and P. Lovati, "Single-photon detection beyond 1 μm: Performance of commercially available InGaAs/InP detectors," *Appl. Opt.*, vol. 35, no. 16, pp. 2986–2996, Jun. 1996.

[5] G. Ribordy, J. Gautier, H. Zbinden, and N. Gisin, "Performance of InGaAs/InP avalanche photodiodes as gated-mode photon counters," *Appl. Opt.*, vol. 37, no. 12, pp. 2272–2277, Apr. 1998.

[6] P. A. Hiskett, G. S. Buller, A. Y. Loudon, J. M. Smith, I. Gontijo, A. C. Walker, P. D. Towensend, and M. J. Robertson, "Performance and design of InGaAs/InP photodiodes for single-photon counting at 1.55 μm," *Appl. Opt.*, vol. 39, no. 36, pp. 6818–6829, Dec. 2000.

[7] D. Stucki, G. Ribordy, A. Stefanov, H. Zbinden, J. G. Rarity, and T. Wall, "Photon counting for quantum key distribution with Peltier cooled InGaAs/InP APDs," *J. Mod. Opt.*, vol. 48, no. 13, pp. 1967–1981, Nov. 2001.

[8] M. A. Itzler, R. Ben-Michael, C.-F. Hsu, K. Slomkowski, A. Tosi, S. Cova, F. Zappa, and R. Ispasoiu, "Single photon avalanche diodes (SPADs) for 1.5 μm photon counting applications," *J. Mod. Opt.*, vol. 54, no. 2–3, pp. 283–304, Feb. 2007.

[9] R. Ben-Michael, M. A. Itzler, B. Nyman, and M. Entwistle, "Afterpulsing in InGaAs/InP single photon avalanche photodetectors," in *Dig. LEOS Summer Top. Meet.*, 2006, pp. 15–16.

[10] S. Pellegrini, R. E. Warburton, L. J. J. Tan, J. S. Ng, A. B. Krysa, K. Groom, J. P. R. David, S. Cova, M. J. Robertson, and G. S. Buller, "Design and performance of an InGaAs-InP single-photon avalanche diode detector," *IEEE J. Quantum Electron.*, vol. 42, no. 4, pp. 397–403, Apr. 2006.

[11] Y. Kang, H. X. Lu, Y.-H. Lo, D. S. Bethune, and W. P. Risk, "Dark count probability and quantum efficiency of avalanche photodiodes for single-photon detection," *Appl. Phys. Lett.*, vol. 83, no. 14, pp. 2955–2957, Oct. 2003.

[12] K. A. McIntosh, J. P. Donnelly, D. C. Oakley, A. Napoleone, S. D. Calawa, L. J. Mahoney, K. M. Molvar, E. K. Duerr, S. H. Groves, and D. C. Shaver, "InGaAsP/InP avalanche photodiodes for photon counting at 1.06 μm," *Appl. Phys. Lett.*, vol. 81, no. 14, pp. 2505–2507, Sep. 2003.

[13] J. P. Donnelly, E. K. Duerr, K. A. McIntosh, E. A. Dauler, D. C. Oakley, S. H. Groves, C. J. Vineis, L. J. Mahoney, K. M. Molvar, P. I. Hopman, K. E. Jensen, G. M. Smith, and S. Verghese, "Design considerations for 1.06- μm InGaAsP-InP Geiger-mode avalanche photodiodes," *IEEE J. Quantum Electron.*, vol. 42, no. 8, pp. 797–809, Aug. 2006.

[14] K. E. Jensen, P. I. Hopman, E. K. Duerr, E. A. Dauler, J. P. Donnelly, S. H. Groves, L. J. Mahoney, K. A. McIntosh, K. M. Molvar, A. Napoleone, D. C. Oakley, S. Verghese, C. J. Vineis, and R. D. Younger, "Afterpulsing in Geiger-mode avalanche photodiodes for 1.06 μm wavelength," *Appl. Phys. Lett.*, vol. 88, no. 13, pp. 133503-1–133503-3, Mar. 2006.

[15] E. A. Dauler, P. I. Hopman, K. A. McIntosh, J. P. Donnelly, E. K. Duerr, R. J. Magliocco, L. J. Mahoney, K. M. Molvar, A. Napoleone, D. C. Oakley, and F. J. O'Donnell, "Scaling of dark count rate with active area in 1.06 μm photon-counting InGaAsP/InP avalanche photodiodes," *Appl. Phys. Lett.*, vol. 89, no. 11, pp. 111102-1–111102-3, Sep. 2006.

[16] M. A. Itzler, X. Jiang, R. Ben-Michael, K. Slomkowski, M. A. Krainak, S. Wu, and X. Sun, "InGaAsP avalanche photodetectors for non-gated 1.06 μm photon-counting receivers," *Proc. SPIE*, vol. 6572, pp. 65720G-1–65720G-10, May 2007.

[17] F. Zappa, P. Lovati, and A. Lacaita, "Temperature dependence of electron and hole ionization coefficients in InP," in *Proc. Int. Conf. Indium Phosphide and Related Materials (IPRM)*, Apr. 1996, pp. 628–631.

[18] S. Adachi, "Optical dispersion relations for GaP, GaAs, GaSb, InP, InAs, InSb, $Al_xGa_{1x}As$ and $In_{1-x}Ga_xAs_yP_{1-y}$," *J. Appl. Phys.*, vol. 66, no. 12, pp. 6030–6040, Dec. 1989.

[19] R. H. Kingston, "Electroabsorption in GaInAsP," *Appl. Phys. Lett.*, vol. 34, no. 11, pp. 744–746, Jun. 1979.

[20] R. J. McIntyre, "On the avalanche initiation probability of avalanche diodes above the breakdown voltage," *IEEE Trans. Electron Devices*, vol. ED-20, no. 7, pp. 637–641, Jul. 1973.

[21] I. Vurgaftman, J. R. Meyer, and L. R. Ram-Mohan, "Band parameters for III-V compound semiconductors and their alloys," *J. Appl. Phys.*, vol. 89, no. 11, pp. 5815–5875, Jun. 2001.

[22] S. R. Forrest and O. K. Kim, "Deep levels in $In_{0.53}Ga_{0.47}As$/InP heterostructures," *J. Appl. Phys.*, vol. 53, no. 8, pp. 5739–5745, Aug. 1982.

[23] O. Wada, A. Majerfeld, and A. N. M. M. Choudhury, "Interaction of deep-level traps with lowest and upper conduction minima in InP," *J. Appl. Phys.*, vol. 51, no. 1, pp. 423–432, Jan. 1980.

[24] D. S. Bethune, W. P. Risk, and G. W. Pabst, "A high-performance integrated single-photon detector for telecom wavelengths," *J. Mod. Opt.*, vol. 51, no. 9–10, pp. 1359–1368, Jun. 2004.

[25] F. Zappa, A. Lotito, A. C. Giudice, S. Cova, and M. Ghioni, "Monolithic active-quenching and active-reset circuit for single-photon avalanche detectors," *IEEE J. Solid-State Circuits*, vol. 38, no. 7, pp. 1298–1301, Jul. 2003.

Xudong Jiang received the B.S., M.S., and Ph.D. degrees in physics from Peking University, China, in 1989, 1992, and 1995, respectively.

He performed postdoctoral work with Harvard University (1995–1996) and Princeton University (1996–1997), working on electrical and optical properties of superlattices and thin-film transistors. He joined the University of Florida as Coprincipal Investigator on a project funded by the U.S. Army Research Office and focused on MWIR and LWIR quantum-well infrared photodetectors (QWIPs) design, processing, and characterization during 1997–2000. He joined Multiplex Inc. in 2000 as a Member of Technical Staff and became a Distinguished Member of Technical Staff in 2002 and Manager of the laser engineering and operation in 2003, working on the development and manufacturing of 980–nm pump lasers and electroabsorption modulated laser (EML) chips and modules. He joined Princeton Lightwave Inc., Cranbury, NJ, in 2006 as a Senior Staff Engineer to work on the design, analysis, and characterization of photodetectors.

Mark A. Itzler (M'96–SM'07) received the B.S. degree in physics from Brown University, Providence, RI, in 1986, and the Ph.D. degree in physics from the University of Pennsylvania, Philadelphia, PA, in 1992.

Following doctoral work at the University of Pennsylvania and Princeton University, he held a postdoctoral research appointment with Harvard University, Cambridge, MA, from 1992 to 1995 to continue his work on low-temperature superconductors. In 1996, he joined Epitaxx Optoelectronics Inc., where he began research and development on near-infrared photodetectors. He provided direct technical leadership for highly successful programs for the development of avalanche photodiodes for 2.5- and 10-Gb/s telecommunications receivers, and, in 1999, he became Director of R&D. Following the acquisition of Epitaxx by JDS Uniphase, he became Chief Technical Officer and Vice President of Device Engineering at JDS Uniphase. In this capacity, he oversaw the design and fabrication of all device-level photodetector technology. In 2003, he became Chief Technical Officer with Princeton Lightwave Inc., Cranbury, NJ, where he continues to develop high-performance photodetector technology and provides oversight for the company's other device technology programs. He has authored approximately 35 technical papers and conference presentations.

Dr. Itzler has been a member of the IEEE LEOS Technical Committee on Photodetectors and Imaging, including three years as the Technical Committee Chair during 2002–2004. He is active in the photodetector community as a conference organizer and guest editor.

Rafael Ben-Michael received the B.A., M.S., and Ph.D. degrees in physics and electro-optics from the Technion-Israel Institute of Technology, Haifa, Israel, in 1987, 1989, and 1993, respectively, where he worked on strained-layer quantum-well InGaAs–GaAs lasers.

In 1993, he joined Bell Laboratories for a postdoctoral position to continue his work on InP-based lasers and photonic integrated circuits. At Bell Laboratories, he pioneered an optical beam expansion device design that was integrated into a waveguide photodetector, an electroabsorber modulator, and a combined laser–modulator–detector photonic integrated circuit. From 1996 to 2000, he held various technical and later technical-management positions with AT&T Laboratories and AT&T Local Network Technology, where he worked on various projects from optical networking to packetized voice-over data networks. Early in 2001, he joined the Epitaxx division of JDS Uniphase as a Device Design Manager. In this role, he was responsible for the development of 40-GHz PIN photodetector and the continuous improvement of APDs to improve APD performance and to tailor APD design parameters to different applications. He joined Princeton Lightwave Inc., Cranbury, NJ, in 2004 as a Principal Scientist developing high-performance photodetector and laser technology.

Krystyna Slomkowski received the B.A. degree in microbiology from Rutgers University, New Brunswick, NJ, in 1976.

In 1978, she joined Laser Diode Laboratories as a Senior Process Technician and was responsible for all processing of GaAs Burrus LEDs. In 1985, she

joined Epitaxx Optoelectronics Inc. as a Senior Process Engineer. At Epitaxx, she was responsible for the process development of planar InGaAs-InP p-i-n photodiodes and establishing a manufacturing line for this product. In 1989, she joined the R&D Development Group at Epitaxx. During this time, she was responsible for developing new processes and product platforms for fiber-optic detectors and receiver packages and supporting and improving existing wafer fabrication processes. In 1999, she was promoted to Technical Manager leading the Process Development Group at the Epitaxx Division of JDS Uniphase. She managed the R&D Process Development professional staff in the daily activities of the development of new processes and platforms for photodiodes. She had management responsibility for all next-generation photodetector process development, and successful programs included efforts on 10-Gb/s APDs and 40-Gb/s PIN detectors. In January 2004, she joined Princeton Lightwave Inc., Cranbury, NJ, as a Senior Staff Engineer, where she is responsible for photodetector and laser diode process development and execution.

Michael A. Krainak received the B.S. degree in electrical engineering from Catholic University, Washington, DC, and the M.S. and Ph.D. degrees in electrical engineering from Johns Hopkins University, Laurel, MD. His doctoral research was on real-time holography and electron transport in photorefractive crystals.

He began his career as a Telephone Switch Office Field Engineer for AT&T Western Electric. He was with the National Security Agency for ten years, where his work involved signal processing, Fourier optics, optical computing, and integrated circuit design. He had a short sabbatical with AT&T Bell Laboratories in the Optical Computing Laboratory of Dr. A. Huang. Recently, he spent a year as the Test and Reliability Manager at Quantum Photonics Inc. For the past 15 years, he has been with the Lasers and Electro-Optics Branch of the NASA Goddard Space Flight Center (NASA-GSFC), Greenbelt, MD, where he is involved with inter-satellite laser communications, lidar, fiber gyroscopes, and fiber-optic data systems. He is presently the Head of the Laser and Electro-Optics Branch at NASA-GSFC.

Stewart Wu received the B.S. degree from the State University of New York, Buffalo, in 2003, and the M.S. degree from the State University of Maryland, Baltimore County, in 2007, both in electrical engineering.

He began his career with the Lasers and Electro-Optics Branch of NASA Goddard Space Flight Center, Greenbelt, MD. He is currently working on ytterbium fiber amplifier development.

Xiaoli Sun received the B.E. degree in radio engineering from Taiyuan Institute of Technology, Shanxi, China, in 1982, and the Ph.D. degree in electrical engineering from Johns Hopkins University, Laurel, MD, in 1989.

He was an Associate Research Scientist with Johns Hopkins University before he jointed the NASA Goddard Space Flight Center, Greenbelt, MD, in February 1999, where he was largely involved with free-space laser communication receivers and laser altimeter and atmosphere lidar receivers. He was the Lead Engineer for detector and receiver calibration for the Mars Orbiter Laser Altimeters (MOLA) and the Geoscience Laser Altimeter System (GLAS) on the ICESat mission. He was the Instrument Scientist for the Mercury Laser Altimeter (MLA) and the Lunar Orbital Laser Altimeter (LOLA). He is also involved in a number of research projects for future space-borne laser remote-sensing instrument developments. His main interests of research are photodetectors, receiver performance analysis, and new measurement techniques for laser remote sensing.